Characterizing protein crystal contacts and their role in protein crystallization

Diana Fusco
Program in Computational Biology and Bioinformatics, Duke University, Durham, NC 27708

Jeffrey J. Headd
Lawrence Berkeley National Laboratory, Berkeley, CA 94720

Alfonso De Simone
Division of Molecular Biosciences, Imperial College London, South Kensington SW7 2AZ, United Kingdom

Patrick Charbonneau
Departments of Chemistry and Physics, Duke University, Durham, NC 27708[*]

Crystallography may be the gold standard of protein structure determination, but obtaining the necessary high-quality crystals is akin to prospecting for the precious mineral. The fields of structural biology and soft matter have independently sought out fundamental principles to rationalize the process, but the conceptual differences and the limited crosstalk between the two disciplines have prevented a comprehensive understanding of the phenomenon to emerge. Here we conduct a computational study of proteins from the rubredoxin family that bridges the two fields. Using atomistic simulations, we characterize the crystal contacts, and then parameterize patchy particle models. Comparing the phase diagrams of these models with experimental results enables us to critically examine the assumptions behind the two approaches and to reveal key features of protein-protein interactions that facilitate their crystallization.

Keywords: protein crystallization ; structural biology ; patchy particle model; potential of mean force ; protein phase behavior

The challenges of designing better drugs [1, 2] and biomaterials [3] rest in large part on determining the target proteins' precise structure. Incomplete structural information for a number of biologically important proteins, such as the ribosome [4, 5], also limits our understanding of their function. In spite of the recent advances in NMR techniques [6], X-ray and neutron diffraction crystallography remain the methods of choice for high-precision protein structure determinations. Yet the lack of systematic ways to crystallize proteins limits the applicability of crystallography [7–9]. An understanding of protein crystallization should follow from a detailed description of the protein-protein interactions [7, 10–12]. But although the individual interaction types (e.g. hydrogen bonding, van der Waals, electrostatics, hydrophobic, etc.) are well characterized [13–17], the effect of their collective behavior on protein assembly is still unclear [18].

In the field of structural biology, protein-protein interactions have historically been divided in two categories: *specific* interactions responsible for protein complex formation or for protein-target association, and *nonspecific* interactions, such as those that underlie most proteins' crystallization [19]. Specific interactions are evolutionarily tuned to be free-energetically and geometrically selective. Nonspecific interactions are on average weaker, having possibly evolved as such to prevent pathological aggregation [19, 20]. Crystal contacts, which are one of the main sources of information on nonspecific interactions, were also long considered stochastic, i.e., essentially indistinguishable from randomly selected surface patches [21–23]. Two recent studies suggest otherwise. Cieślik and Derewenda found that crystal contacts are enriched for glycine and small hydrophobic residues, while large polar residues with high side-chain entropy are underrepresented [24]. Price *et al.* found that the proteins with a larger fraction of glycine and alanine on their surface are more likely to have been successfully crystallized [25]. These observations have provided statistical support for the surface entropy reduction (SER) mutagenesis approach, which recommends replacing high-entropy surface residues with alanine to ease crystal formation [26, 27]. More importantly, they reveal that crystal contacts are not completely stochastic.

In the field of soft matter, the observation that short-range isotropic attraction between particles results in a gas-liquid critical point that lies below the crystal solubility regime [28, 29] suggested an analogy for the solution behavior of proteins [30–32]. In these systems, successful crystallization can most easily be achieved in the region between the solubility line, above which the system does not aggregate because the disperse phase is stable, and the critical point, below which the system typically forms "amorphous" materials that are useless for crystallography [33]. The enhancement of homogeneous nucleation rates in the critical region [34–36] further gave a physical basis to George and Wilson's observation that a small second virial coefficient is a predictor of the nucleation zone of globular proteins [37]. Though appealing in their simplicity, isotropic interactions between proteins

---

[*] corresponding author: patrick.charbonneau@duke.edu

were soon proven too simplistic to explain certain solubilization trends [30, 38–41]. In response, a broad array of schematic models with anisotropic, directional attraction, i.e., "patchy" models, were developed [42, 43].

Despite the convergence between the structural biology and the soft matter research lines on the relevance of interaction anisotropy for protein crystallization, a large conceptual gap remains to be filled before reliable experimental guidance can be provided. In particular, although anisotropy plays a key role in crystallization [44–46], little characterization of the interaction between crystal contacts has been done [47], leaving most of the physical assumptions behind patchy models untested.

In this article, we use classical atomistic simulations to characterize the anisotropy in the crystal contact interactions of three closely related small globular proteins from the rubredoxin family: (a) the wild-type from *Pyrococcus furious* (wt-RbPf, PDB code: 1BRF) [48], its (b) W3Y/I23V/L32I mutant (mut-RbPf, PDB code: 1IU5) [49] and (c) the W4L/R5S mutant from *Pyrococcus abyssi* (mut-RbPa, PDB code: 1YK4) [50]. These proteins from hyperthermophilic organisms, which are known for their extended temperature stability, provide a natural model system for our study. Through a comparative analysis, we identify the molecular basis of their interactions, and parameterize patchy models whose phase diagrams are then compared with experimental crystallization conditions. The validity of our approach is supported by the recent success of multiscale descriptions of protein aggregation [51]. By showing that the models and the experimental results agree fairly well, we (i) conclude that increasing the temperature may sometimes produce higher resolution crystals, (ii) suggest a microscopic interpretation for SER and, (iii) offer a framework for developing relevant patchy models for protein crystallization.

I. RESULTS AND DISCUSSION

Using umbrella sampling simulations (Methods, Appendix B), we characterize the solvated protein-protein interaction as a function of the center of mass-center of mass (COM-COM) distance and of the protein's relative orientation for each crystal contact (1, 2, and 3) (Fig. 1).

A. Crystal contacts of wt-RbPf and mut-RbPf

The orientationally-constrained potential of mean force (PMF) of wt-RbPf is first obtained in pure water solution (Fig. 1A). All three contacts are strongly repulsive below 2.2 nm, which defines the protein diameter σ. The PMF minimum for interface 1a and 3a matches the observed crystal distance, and unsurprisingly the strength of the interaction correlates with the size of the interface (Fig. A.3). Otherwise, the interfaces share little in common. Interface 2a is either repulsive or neutral, while

interface 1a is attractive and relatively long-range (up to 3 nm) and interface 3a is attractive and short-range (up to 2.45 nm). The relative abundance of hydrophobic regions in interfaces 1a and 3a compared to interface 2a (Fig. A.4) [53, 54] suggests that this effect dominates the assembly. The range difference between the PMF of interfaces 1a and 3a can be explained by the stabilization of the former by a pair of hydrogen bonds between the C-terminus tail of one chain and a loop on the other. The tail's flexibility extends the attraction to larger distances. Interestingly, the PMF of other reasonably attractive orientations result in interfaces that are essentially inaccessible due to the presence of high intermediate entropic barriers (Appendix B, Fig. A.7). The crystal contacts are therefore clearly not purely stochastic nor isotropic.

The N-terminal methionine and formylmethionine variants (PDB codes: 1BQ8, 1BQ9) [48] were crystallized under identical experimental conditions and show similar crystal structures, because the mutated region is not involved in any crystal contact. The core mutations of mut-RbPf also result in a similar crystal form. Because of the low resolution of the C-terminus tail in this protein, the last two residues (Glu52 and Asp53) were not included in the PDB file (1IU5). Instead of assigning them a position, we choose to characterize the pair-wise interaction in the absence of the C-terminus in order to assess whether its presence is necessary for crystal formation. Interface 1b (equivalent to 1a) is most affected by the tail's removal. Without it, the interface area is smaller and the interaction weaker by about 7 kJ/mol than in the wild-type (Fig. 1B), which indeed affects crystal formation, as we find below.

B. Crystal contacts of mut-RbPa

Mut-RbPa has substantially different crystal contacts from the previous two proteins. Although each chain has six nearest neighbors, only four of them (forming two interfaces) are sufficiently close to contribute to the pair attraction (Fig. 1C). The resulting distance at crystal contact for interface 1c is congruent with the minimum of the PMF (solid), but 2c's distance in the crystal is slightly smaller than the PMF minimum. This last discrepancy might be due to a slight compression of the sample upon its freezing for data collection, as we do not detect any protein distortions associated with the restraints placed on the iron site sitting opposite to the interface (Fig. A.5). In any case, the difference is rather small and the overall interaction free energy minimum is consistent with the crystallization conditions, as we find below. The hydrophobic component on interface 1c is relatively small. The attraction is dominated by a salt-bridge between Arg50 and Asp35, which is stable between 1.9 and 2.1 nm, while at larger distances water fills the gap between the two proteins. The PMF therefore first plateaus, then rapidly increases (Fig. 1C).

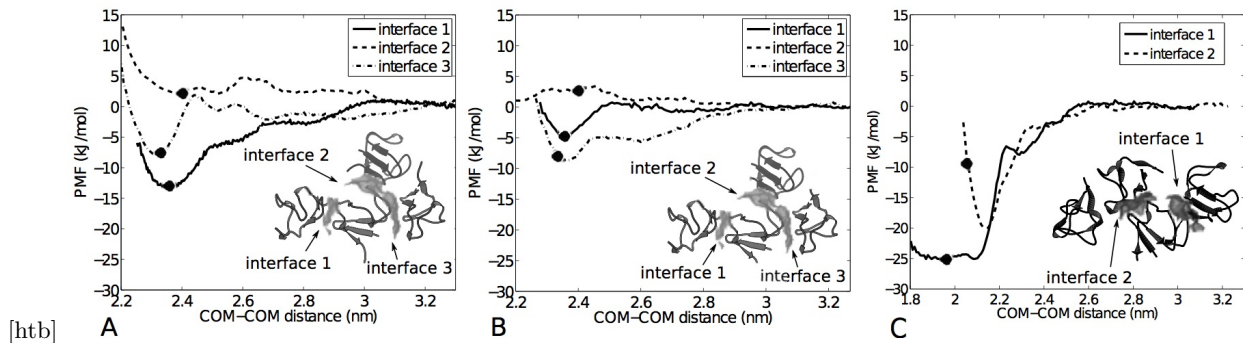Assuming that the strongest pair interaction typically

FIG. 1. PMF for wt-RbPf (A), mut-RbPf (B) and mut-RbPa (C). The black circles indicate the COM-COM distance in the crystal. The interface surfaces between neighboring proteins identify the pair-wise interactions of residues involved in crystal contacts [52].

forms first in a nucleation process, one may wonder why interface 1a in wt-RbPf is absent from the crystal contacts of mut-RbPa and vice-versa. In particular, interface 1c is at least twice as strong as any interface of wt-RbPf, so one may wonder why it is missing from the crystal contacts of wt-RbPf and its mutants. Interface 1c is characterized by the absence of the C-terminus and the mutation of Lys50 to arginine. Deleting the C-terminus allows the two chains to fit closely together and the arginine residue to form a salt bridge with Asp35 (Fig. A.9A). To test whether the creation of this new interface can be attributed to the shorter tail of mut-RbPa, we delete the C-terminus of wt-RbPf and fit the two chains to the structure of interface 1c (Fig. A.9B). The PMF indicates that the interaction between the two chains is still neutral (Fig. A.9C), i.e., lysine and arginine are not here interchangeable. Closer examination reveals that both the nitrogen groups of arginine interact with the other chain through a salt bridge and a hydrogen bond. Conversely, lysine offers a single nitrogen group to compete with solvation. The latter process is found to dominate, in agreement with lysine's solvation free energy being nearly twice more negative than that of arginine [55].

C. Patchy particle models and phase diagrams

In order to estimate the phase diagram of these proteins and to identify the facile crystallization regime, we use a coarse-grained model hybrid between Sear's [56] and Kern-Frenkel's [44]. The proteins are represented as particles with a hard core of diameter σ decorated by $n=2$ or 3 pairs of surface attractive patches that each schematize a solvent mediated crystal contact (Fig. 2A-B, Methods). The parameters of the models are extracted from the MD simulations above (Table I), and the phase diagrams are computed using advanced Monte Carlo methods [57] (Fig. 3, Methods, Appendix C). The solubility lines (S/F) mark the coexistence condition between solvated and crystallized proteins, while the gas-liquid lines (G/L) identify the condition under which high and low concentration solutions of proteins can coexist. As expected from the relatively short range of the attraction ($\sim 5-10\%\sigma$), in all cases the gas-liquid coexistence line is metastable with respect to crystallization. Observed relative variations of the attraction width (between 1 and 5%) and range (between 5 and 10%σ) only change the melting temperature up to 3% and the critical temperature up to 8%, which supports robustness of the model in the crystallization zone.
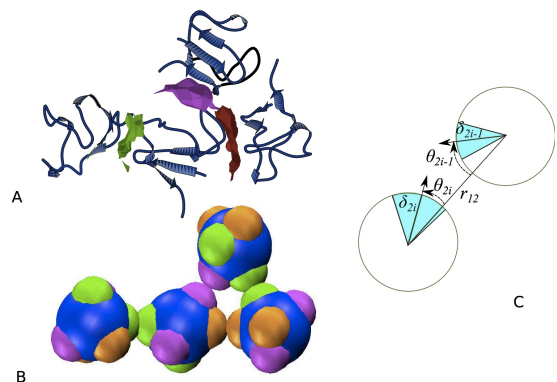

FIG. 2. Coarse-grained representation of the protein crystal (A) through a patchy particle model (B). The blue spheres are proteins on which each pair of patches corresponds to the crystal interface of the same color. C: schematic of the interaction between two particles through patch $2i$ and patch $2i-1$. The colored region represents the angular width of the patch.

We find the temperature at which mut-RbPa was experimentally crystallized (293 K) to be very near the model's critical temperature. This temperature has been suggested as optimal for crystallization [34], because the density fluctuations associated with criticality enhance the nucleation process. Crystals of mut-RbPf were interestingly detectable after a remarkably short period of 12 hours [50]. Yet whether critical fluctuations facili-

tate crystallization in patchy models remains subject of debate [58]. It is nonetheless worth noting that the wild type of RbPa showed excessive nucleation in the same experimental conditions and was only crystallized (at low resolution) by adding dioxane to the solution [50]. As the crystallization conditions for the mutant are very close to the critical point to begin with, a small perturbation of the protein-protein interaction range and width in the wild type may have been sufficient to tilt it over to the amorphous aggregation region. The patchy model phase diagram, therefore, suggests that increasing the crystallization temperature might have been a better strategy to obtain high-resolution crystals than adding a cosolute.
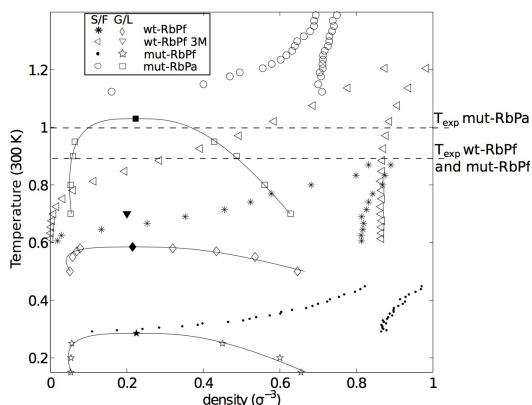

FIG. 3. Phase diagram for wt-RbPf, wt-RbPf at 3 M NaCl, mut-RbPf and mut-RbPa. The solid-fluid lines (S/F) for the three systems are represented respectively by asterisks, left-pointing triangles, points and circles. The gas-liquid (G/L) are indicated by diamonds, down-pointing triangles, stars and squares. The filled symbols identify the critical points. The dashed lines correspond to the temperatures at which the crystallization experiments were conducted.

The identical experimental crystallization conditions for wt-RbPf and mut-RbPf, and for a series of mutants whose crystal contacts are closely related [48, 49], suggest that the phase diagram of the two proteins should be similar. Our removing of the C-terminus tail, which weakens 1b, however, lowers the solubility line well below the experimental crystallization temperature. Although absent from the PDB structure, the C-terminus in the mutant should therefore interact with the other chain similarly as in the wild type for crystallization to be physically possible. We cannot exclude that a mutant of RbPf missing the C-terminus could have the same crystal contacts as the wild type, but were it to be the case our study indicates that such a mutant would not crystallize under the same solution conditions.

D. Effect of high salt concentration on wt-RbPf

Even taking the contribution of the C-terminus into account the experimental crystallization temperature of RbPfs (277 K) is still too high for the obtained phase diagram. A possible source of discrepancy is the difference in NaCl concentration used in the patchy model parameterization compared to the experimental conditions (45 mM vs. $\sim$ 3 M). Salt only weakly perturbs the PMF of interfaces dominated by hydrophobic attraction (within the simulation error, Fig. A.8), in agreement with NaCl being a weak salting-out agent [59], but interface 2a becomes significantly more attractive at 3 M NaCl (Fig. 5). To better understand the origin of this effect, we examine the counter-ion distribution near the interface (see Appendix B). Interface 2 is characterized by the presence of six negatively (two on one chain and four on the other) and three positively (all on a single chain) charged residues. It is thus highly hydrated, as both the PDB structure (1BRF) and the simulations illustrate. The overall electrostatic repulsion between the two proteins at this interface is only weakly screened at low salt concentration, but quite screened at high salt concentration. Under the latter conditions, the positively charged residues at the edge of the interface are accessible to the ions and are therefore screened, but the negatively charged residues buried in the core of the interface are not. As a result, like charge repulsions between residues on different proteins and positive-negative attractive interactions between residues on the same protein are screened, but the unlike charges on different proteins at the core of the interface are essentially unscreened, generating an effective attraction between the two chains (Fig. 4). More specifically, when no ions are present, the positively charged Lys6 interacts with Glu49 on the same chain and not with the polar carboxyl of Gly22 on the other chain. If the concentration of salt increases, Glu49 is entirely screened by counter ions beyond 2 Å (black solid line), but both Lys6 and Gly22 still interact with each other.

Reparameterizing the patchy model's interface 2a brings the phase diagram of wt-RbPf in remarkably close agreement with the experimentally observed crystallization conditions (Fig. 3).

II. THEORETICAL ASSESSMENT

From this proof-of-concept study, we draw microscopic insights about both the underlying structural biology and soft matter motivations.

A. Surface Entropy Reduction

One of the main insights obtained from the statistical study of crystal contacts is that surface entropy reduction should facilitate crystallization. The approach has been successfully used to crystallize proteins in various
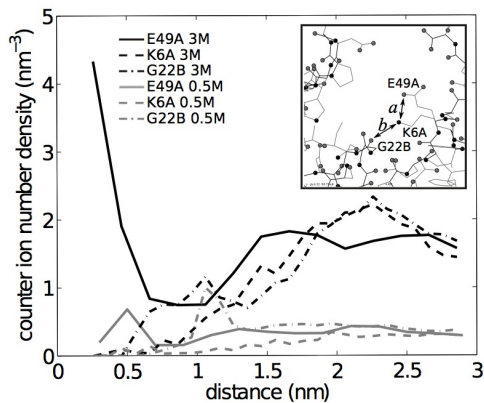
FIG. 4. Number density of counter ions as a function of distance from the charge of three different residues: Glu49 on chain A (solid), Lys6 on chain A (dashed) and the oxygen of Gly22 on chain B (point-dashed). Black lines refer to the 3M NaCl simulations, grey lines to the 0.5 M NaCl simulations. The inset shows the location of the residues at crystal contact. At low salt concentration Glu49 interacts with Lys6 on the same chain (arrow a), while at higher salt concentration Glu49 is screened and Lys6 interacts with the carboxyl group of Gly22 on the other chain (arrow b).
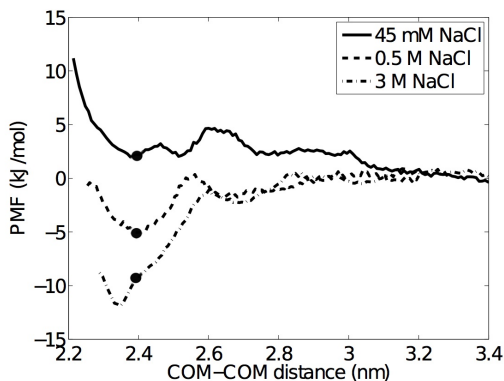

FIG. 5. PMF of interface 2 for wt-RbPf at different salt concentrations.

contexts [10] and to rationalize the results of other studies [60]. Yet it is not universal, and has but a weak microscopic justification. The method is reasonable for interactions driven by hydrophobicity, which are disrupted by the presence of polar or charged residues [61], or for interactions characterized by backbone-backbone hydrogen bonding, which are favored by the presence of small residues. For crystal contacts with polar side-chain interactions, however, the mutation/deletion of highly-entropic residues may have less straightforward effects.

(i) Mutating the highly-entropic charged residues may weaken protein-protein interactions, because it deletes the source of favorable salt bridges between chains. In interface 1c of mut-RbPf the mutation of either Arg50 or Asp35 to an alanine would break the salt-bridge, desta-

bilize the main attractive patch, and possibly prevent crystallization. The observation that in this interface lysine and arginine are not interchangeable, in spite of their similar conformational entropy and their net charge, also shows that entropic effects should not be considered in isolation. In this specific case, the different propensity of forming multiple bonds and the solvation free energy play key roles in distinguishing the effect of the two residues.

(ii) For wt-RbPf, the SER method specifically recommends mutating Glu49 into alanine [27]. As observed in the analysis of interface 2a, the electrostatic interaction of Glu49 with Lys6 at low salt concentration prevents the inter-chain interaction between Lys6 and Gly22 and therefore crystallization. Mutating Glu49 would delete the responsible charge and potentially strengthen the pair-interaction by an alternate route than increasing the salt concentration. In this situation, the suggested mutation would likely help crystal formation not because it specifically reduces the surface entropy, but because it changes the electrostatic potential at the interface (Fig. A.10).

(iii) Entropy reduction more generally can have counter-productive effects on protein crystallization. A clear example is provided by the comparison of interface 1a and 1b when the C-terminus of wt-RbPf is deleted. This region of the chain, being very flexible, increases entropy so one may postulate that its deletion should facilitate crystallization. The phase diagram of truncated mut-RbPf shows instead a drop of the solubility line that prevents crystallization under the same conditions as for the wild type because of hydrogen-bond deletion.

Although a useful starting point, it thus appears that the SER approach could be greatly improved if additional information were considered. In particular, the nature of the surrounding amino acids along the chain might help identify residues that are weakening interactions by disrupting hydrophobic patches or by competing with favorable inter-chain interactions.

B. Patchy models

The central premise that the phase behavior of crystallizing proteins could be understood from that of particles with short-range anisotropic interactions is here verified, at least for compact globular proteins. The typical regime for successful experimental crystallization is intermediate between the metastable critical point and the solubility line at low to intermediate protein concentration, which results in open crystal structures dominated by directional interactions.

It is well understood by now that reducing the range and surface coverage of attraction lowers the critical temperature and broadens the crystallization regime [43, 44, 62]. Yet whatever role the critical point may have in assisting nucleation [34, 58] is of little relevance if the protein is highly soluble. Our study shows that in water, RbPf and its mutants, for instance, do not crystallize

because the solubility line lies at very low temperatures or high densities. The addition of salt to the solution strengthens the pair-wise interaction, but does not significantly affect its range or width, except for unscreened electrostatic interactions. The pair interactions thus naturally results in an attraction range that lies between 1 and 3 Å, and a larger protein would shrink the fraction of the protein diameter σ over which the attraction is felt. Although tightening the fractional range by an order of magnitude dramatically affects the critical point, it only weakly perturbs the position of the solubility line. If anything, crystallization should therefore become easier. The parameter that most controls the solubility is the strength of the interaction. The phase diagram in Fig. 3 shows that to achieve reasonable solubility at room temperature, the average interaction strength per patch should be of order 8 kJ/mol for a protein with six crystal contacts and of 20 kJ/mol for a protein with four.

In patchy particle models, modifying the strength of the interaction is equivalent to rescaling temperature: a stronger interaction maps the same phase diagram to higher temperatures. From a practical point of view, tuning the strength of the interaction, however, is quite difficult to achieve and typically requires a detailed microscopic understanding. Our simulations show that even small details, such as mutating a lysine to an arginine, or the preferential screening observed at high salt concentration, can significantly affect the interaction, urging for more systematic atomistic-level studies in this direction.

A common assumption in patchy particle models is that the patch-patch interactions responsible for crystallization are essentially identical. Our simulations clearly show it not to be the case in proteins. Comparing the phase diagram of wt-RbPf and mut-RbPa indicates that it may be more efficient to have more weak patches than fewer strong patches, in order to decrease the solubility of a protein. If we rescale the temperature over the average energy per particle in the crystal ($\sim$10 $k_B T$ for wt-RbPf and $\sim$18 $k_B T$ for mut-RbPa), the solubility line of mut-RbPa drops below that of wt-RbPf, indicating that mut-RbPf is crystallized by making up for the absence of an interface by having a drastically increased attraction strength for the others. This observation raises the question of how the distribution of energy across patches affects the phase diagram, which has so far received little attention.

In this paper, we have studied the interaction of three closely related proteins of the rubredoxin family using an approach that bridges structural biology and soft matter descriptions of protein crystallization. It allowed us to characterize representative values of protein-protein interactions and to obtain reasonable phase diagrams, providing a microscopic explanation as to why certain simple mutations dramatically affect the crystallization behavior. The analysis even offers predictive capabilities. Overall, this approach is well-suited for simple proteins, especially those for which some structural information is available from analogs. Besides the increased

computational cost, considering more complex proteins would require the introduction of additional features to the schematic models. For example, some proteins assemble in more than one crystal form and consequently should be characterized by a larger set of patches. The position of the patches may also not be kept fixed if conformational changes occur on a timescale similar to crystallization. Further work in this direction could be fruitful from both a theoretical and an experimental point of view.

III. METHODS

A. Molecular Dynamics simulations

Molecular dynamics (MD) simulations are performed with the Gromacs package [63] using the Amber99sb forcefield [64] and explicit TIP4P water [65] with Ewald summation. Preliminary simulations revealed problems in the stability of the protein around the iron site (Fig. A.1), which are corrected with chemically justified constraints (Appendix B). The corrected MD recapitulates experimental data (Fig. A.2). The PMF as a function of radial distance is obtained with the umbrella sampling and weighted histogram package implemented in Gromacs [66]. Separate simulations are run to resolve the angular dependence of the interaction and to analyze the ions behavior around the crystal contacts (Appendix B).

B. Patchy particle model

We use a patchy particle model, where each particle carries $i = 1, \ldots, n$ pairs of patches. Patch $2i$ interacts only with $2i - 1$, as in the Sear's model [56], while the range and width of the interactions are independent parameters, as in the Kern-Frenkel model [44]. In contrast to both Sear's and Kern-Frenkel's models, which assume the same interaction for each pair of patches, we allow the interaction to change from one pair of patches to the other, capturing the pair-wise nature of interaction at the crystal contact.

The pair-wise interaction between particles 1 and 2, whose centers are a distance r_{12} apart, is

$$\phi(r_{12}, \Omega_1, \Omega_2) = \phi_{HS}(r_{12}) + \sum_{i=1}^{n}[\phi_{2i,2i-1}(r_{12}, \Omega_1, \Omega_2) + \phi_{2i-1,2i}(r_{12}, \Omega_1, \Omega_2)], \quad (1)$$

where Ω_1 and Ω_2 are the Euler angles. A hard-sphere (HS) potential captures the volume exclusion

$$\phi_{HS} = \begin{cases} \infty & r \leq \sigma \\ 0 & r > \sigma, \end{cases} \quad (2)$$

where σ is the diameter of the particle. The patch-patch interaction is the product of a radial and an angular component

$$\phi_{2i,2i-1}(r_{12}, \Omega_1, \Omega_2) = \psi_{2i,2i-1}(r_{12})\omega_{2i,2i-1}(\Omega_1, \Omega_2), \quad (3)$$

where

$$\psi_{2i,2i-1} = \begin{cases} -\epsilon_i & r \leq \lambda_i\sigma \\ 0 & r > \lambda_i\sigma \end{cases} \quad (4)$$

and

$$\omega_{2i,2i-1}(\Omega_1, \Omega_2) = \begin{cases} 1 & \theta_{1,2i} \leq \delta_{2i} \text{ and } \theta_{2,2i-1} \leq \delta_{2i-1} \\ 0 & \text{otherwise} \end{cases}. \quad (5)$$

The range of the interaction λ_i is in units of σ between patch $2i$ and patch $2i - 1$, δ_{2i} is the semi-width of patch $2i$ and $\theta_{1,2i}$ is the angle between the vector r_{12} and the vector defining patch $2i$ on particle 1, as illustrated in Fig.2C. An analogous definition holds for $\theta_{2,2i-1}$.

The parameters of this model are obtained from the MD simulations (Table I). The depth of the well ϵ corresponds to the minimum of the PMF and the effective interaction range λ_i is such that the second virial coefficient of the modeled interaction matches the actual protein-protein interaction at the crystal contact. The angular distribution of the configurational space sets the width of the patches (Fig. A.6), under the constraint that $\sin(\delta_{2i}) < (2\lambda_i)^{-1}$ to guarantee that each patch forms no more than one bond.

C. Phase diagram

The gas-liquid line of the phase diagram is obtained using the Gibbs ensemble method [67] and the critical temperature and density using the law of rectilinear diameters [68]. The solubility line is computed integrating the Clausius-Clapeyron equation starting from a first coexistence point, determined using free energy calculations and thermodynamic integration [57, 68] (Appendix C).

ACKNOWLEDGMENTS

Appendix A: Crystal reconstruction and interface determination

The three proteins studied share the same low-symmetry space group $P2_12_12_1$, and a single chain is present in the asymmetric unit for all investigated structures. The package XPAND[69] is used to reconstruct the

-	wt-RbPf	mut-RbPf	mut-RbPa
$\sigma(nm)$	2.2	2.2	2
λ_1 (σ)	1.09	1.05	1.06
ϵ_1 (k_BT)	5.5	2	10.03
$\cos(\delta_1)$	0.97	0.97	0.93
$\cos(\delta_2)$	0.94	0.94	.89
λ_2 (σ)	1.1	1.1	1.04
ϵ_2 (k_BT)	0.2	0.2	8.02
$\cos(\delta_3)$	0.9	0.9	0.95
$\cos(\delta_4)$	0.89	0.89	0.92
λ_3 (σ)	1.05	1.05	-
ϵ_3 (k_BT)	4.35	4.35	-
$\cos(\delta_5)$	0.89	0.89	-
$\cos(\delta_6)$	0.89	0.89	-

TABLE I. Model parameters for wt-RbPf and mut-RbPa

crystal. The first neighbors of each protein are manually determined with direct visualization and the interface between two neighboring proteins was built using Ciel [52].

Appendix B: Molecular dynamics (MD) simulations

Due to the lack of a parameterization for the iron atom in the forcefield, we bind the iron to the rest of the protein by treating the Fe-S bonds as covalent bonds in the topology file. The simulation box for each kind of MD is prepared as follows: water and ions are added to the protein, followed by energy minimization (steepest descent integrator) and equilibration at constant volume for 100 ps with position restraints on the heavy atoms (O, C, S and N). The MD simulations described in the following sections are then run with the parameters reported in table A.1, using the first ns as equilibration. Although the simulations are all run at 300 K, the PMF results hold in a surrounding temperature range, as long as the protein and the solvent do not undergo major conformational or physical changes.

1. Protein stability

We first test the adequacy of the forcefield running unconstrained simulations of a single copy of each protein in solution for 10 ns (individual unconstrained MD). Unsurprisingly, the forcefield fails in representing the dynamics of the protein around the iron. All three protein structures undergo a large conformational change after about 4 ns in which the loop between residues 35 and 45 opens due to a shift of the segment between residue 41 and 48 (Fig. A.1 and Fig. A.2A) and the breakage of several hydrogen bonds that should nominally be stable [70]. This behavior is in disagreement with both the B-factor in the PDB file (PDB code: 1BRF) [48] and the root mean square deviation (rmsd) in NMR studies (PDB

Parameter	Value
Forcefield	Amber99sb
Water model	Tip4pEW
Temperature	300 K
Temperature control	Nosé-Hoover thermostat
Pressure	1 bar
Pressure control	Parrinello-Rahman barostat
Box dimension	6 nm×6 nm×12 nm
Electrostatic method	PME
Coulomb radius	1.4 nm
Van der Waals method	Cut-off
Van der Waals radius	1.4 nm
Integration step	2 fs
Constraint algorithm	Lincs
Salt concentration	45 mM/3 M of NaCl

TABLE A.1. MD simulations parameters

code: 1ZRP) [71] that do not report strong fluctuations in this region (Fig. A.2B). It is unclear if the discrepancy is caused by an artifact due the artificial restraints that we use to bind the iron atom to the protein, by a poor parameterization of the cysteine by the forcefield when the metal is present, or by the failure of the forcefield to capture the behavior of more subtle interactions around the site [70]. Changing forcefield (CHARMM) [72] and water model (TIP3P) does not improve the results. To address this problem we introduce additional constraints on the NH$\cdots$S hydrogen bonds length [70] near the iron using a harmonic potential with spring constant equal to 10000 kJ/(mol nm^2). Because these constraints do not affect the surface of the protein involved in crystal contacts, they should not bias our analysis, yet they successfully prevent the conformational change of the protein (Fig. A.1 and Fig. A.2A) and recapitulate the experimental data remarkably well (Fig. A.2C and C). The discrepancy between the high B-factors and low fluctuations in the MDs and NMR for residues 26, 30 and 31 (fig. A.2B) might be caused by some crystal abnormalities. Although no alternate conformations are present, residues 30 and 31 show a considerable amount of negative density, which can be explained by a partial decarboxylation due to radiation damage [73]. A better parameterized refinement of the model to account for this damage could improve the B-factor values.

2. Umbrella sampling to determine the potential of mean force

The umbrella sampling and weighted histogram package implemented in Gromacs [66] are used to determine the PMF at each crystal contact of every protein. The starting configuration for umbrella sampling are generated pulling one protein along the reaction coordinate while keeping the other one fixed. The reaction coordi-
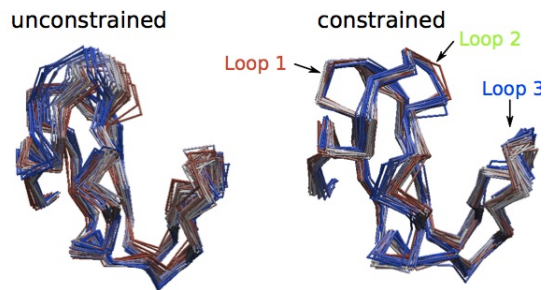

FIG. A.1. C_α trace along a simulation of an individual protein with and without the constrained hydrogen bonds. The color changes from red to blue along the simulation.

nate is identified by calculating the inertia tensor of the interface and its principal axes. Two of the axes define the plane of the interface, and the third, which is orthogonal at the interface, is used as reaction coordinate.

During the pulling, we control the reciprocal orientation of the two proteins as in Ref. [47]. We first determine the four most stable heavy atoms in the structure from individual MD simulations, such that the tetrahedron defined by these four atoms spans most of the protein structure, to be the C_α of Ile7, Pro19, Asp35 and Glu52. For mut-RbPf, we use the C_α of Lys50 instead of Glu52, as the latter residue is not reported in the PDB file. We then restrain the angles between the edges of the two tetrahedra with a spring constant of 1000 kJ/(mol rad^2). These restraints prevent the proteins from rotating with respect to each other, yet allow ample freedom in both backbone and sidechain fluctuations. Fig. A.2B and C compare the fluctuations and the chemical shifts for one of these simulations (first window of interface 1b), for the isolated MDs and for the NMR. Although the fluctuations in the umbrella sampling MD (US MD) are lower than those in the isolated MD, probably because of the presence of another chain close by, they do not show any significant distortion and remain in agreement with the NMR data. The starting configurations are sampled every 1 Å up to a distance of 15 Å with a spring constant of 1000 kJ/(mol nm^2). The simulations are run for a total of 10 ns. These parameters typically provide sufficient overlap between the distributions from each window to perform histogram reweighting. In cases where the PMF gradient is too high, the window size is reduced to 0.5 Å, so as to preserve a reasonable overlap between neighboring windows.

We estimate the accuracy of the umbrella sampling using 100 bootstraps. The resulting standard deviation associated with the minimum of the PMF is between 2 and 3 kJ/mol, which corresponds to a 10-20% relative error for the strength of the interaction. Replicates of the simulations (three) provide a similar estimate. This uncertainty does not include further errors introduced by the limitations of the forcefield, but is in line with the overall robustness of the parameters used for the phase diagram determination.
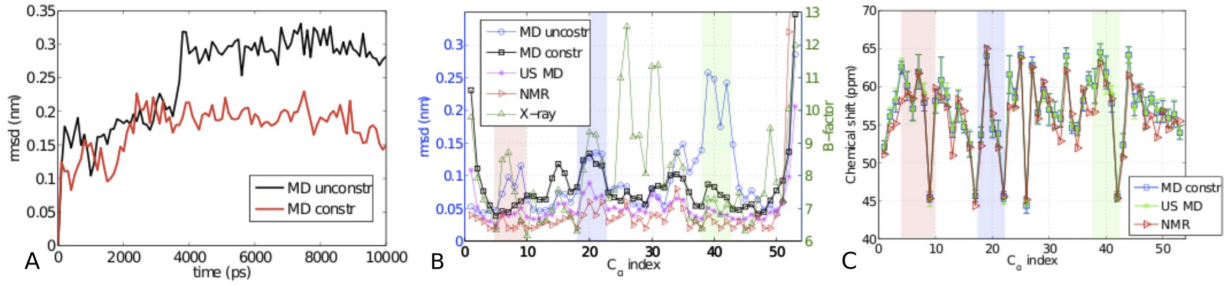
FIG. A.2. Comparison between MD results and experimental data. A: Total rmsd of the C_αs along the individual unconstrained simulation (black) and the individual constrained simulation (red). B: C_α fluctuations in the unconstrained isolated MD simulations (MD uncostr), the isolated MD simulations with constrained hydrogen bonds (MD constr), the umbrella sampling MD simulations (US MD), the NMR fluctuations (NMR, PDB code: 1ZRP) [71] and the B-factor reported in the crystal structure (X-ray, PDB code: 1BRF) [48]. The C_α involved in loop 1, 2 and 3 (Fig. A.1) are highlighted respectively in red, green and blue. C: Chemical shifts and relative standard deviation obtained with SPARTA [74] using 800 frames from the equilibrated constrained isolated MDs and the equilibrated US MD compared with the experimental chemical shifts of the NMR structure [71].
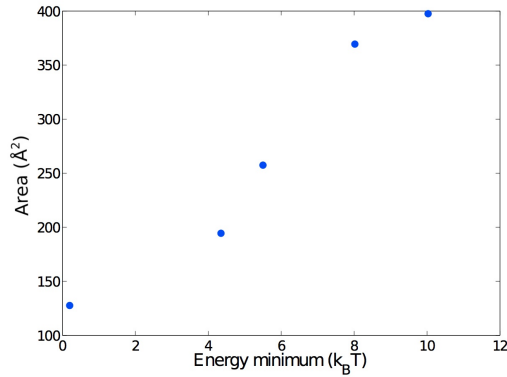

FIG. A.3. Scatter plot of the minimum of the pmf in units of $k_B T$ and the solvation area of the interface for the crystal contacts in wt-RbPf and in mut-RbPa.
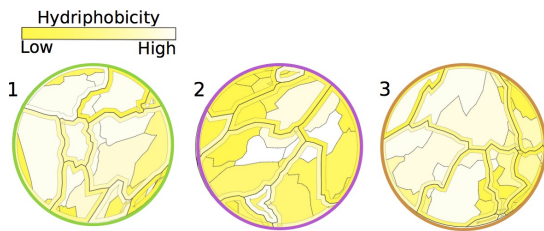

FIG. A.4. Projection of the thee crystal contacts of wt-RbPf labeled as in Fig. 1. Each tile represents a residue involved in the interface colored depending on its hydrophobicity level [54].
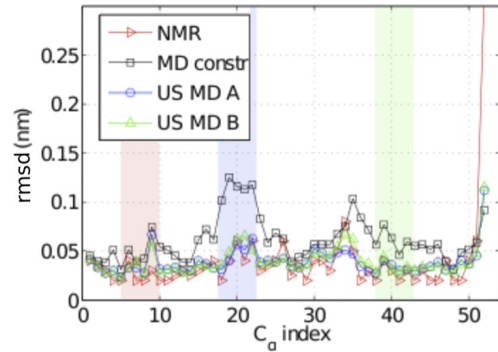

FIG. A.5. Comparison between the rmsd from NMR of wt-RbPf (NMR) [71], from the constrained individual MDs on mut-RbPa (MD constr) and from chain A (US MD A) and chain B (US MD B) in the first umbrella sampling window of interface 2c. The iron site of chain A is involved in the crystal contact. The good agreement between NMR and US MD for both chains in loop 1 and 2 (red and green highlighted regions) suggests that the constraints on the iron do not introduce any detectable distortion and are, consequently, unlikely to be the source of disagreement between the position of the minimum in interface 2c and the distance at crystal contact.

3. Angular dependence of the interaction

In order to investigate the angular component of the interaction, we run four independent 5 ns-long simulations restraining the distance between the centers of mass of the two proteins for each interface with a spring constant of 1000 kJ/(mol nm^2). Assuming that around the crystal contact different configurations are visited according to the Boltzmann distribution, the sampled ensemble of angles provides an estimate of the pair-wise interaction width. Given the model notation (see Methods), we define $\delta_{2i} = \min[\mathrm{asin}(\frac{1}{2\lambda_i}), \mathrm{acos}(1 - 2\tilde{\sigma}_{2i})]$, where $\tilde{\sigma}_{2i}$ is the standard deviation of the $\cos(\delta_{2i})$ distribution obtained with these simulations (Fig. A.6).
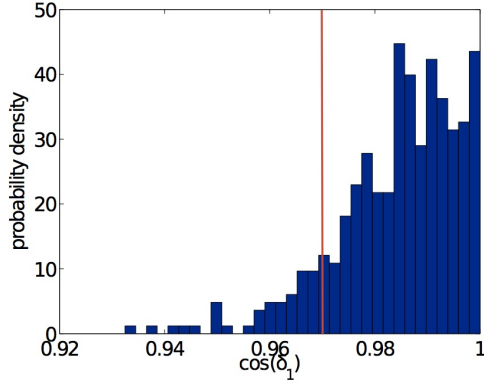
FIG. A.6. Sample determination of the angular width of the interaction. The histogram represents the distribution of $\cos(\delta_1)$ for interface 1a. The red line identifies the position of 2 standard deviations, which is used to parameterize the model.
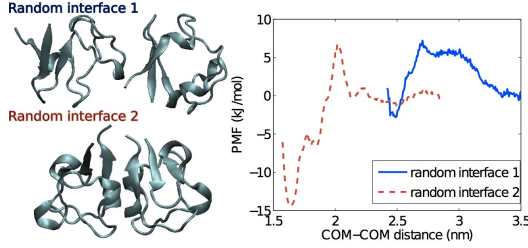

FIG. A.7. PMF of two alternate protein-protein interfaces. Random interface 1 is built using one chain oriented as in interface 1a and one chain oriented as in interface 2a (solid blue line). Random interface 2 is the lowest energy configuration found by RosettaDock (dashed red line). Both show a free energy barrier of about 6 kJ/mol.

4. Alternate orientations and their interaction

To assess the specificity of the crystal contacts, we determine the PMF at two alternate orientations. The first is a hybrid between interface 1a and 2a, which addresses whether one patch interacts only with its partner patch. For the second interface, we use the highest scored configuration found by RosettaDock [75, 76]. Fig. A.7 shows that the first interaction is mostly repulsive and weakly attractive at short range, in support of our patch-specific interactions. The second interaction, although at short range sightly more attractive than interface 1a, is mostly inaccessible because of the high free-energy barrier caused by the entropic cost of immobilizing the two C-termini.

5. Characterization of ion behavior at high salt concentration

To understand the behavior of ions around interfaces at high salt concentration (3 M of NaCl), we perform 4

ns-long MD simulations. We constrain the center of mass of the proteins and their reciprocal orientation to that of the crystal. Frames selected every 20 ps are used to draw statistics over the ions located around the interface. The number density of the ions is obtained normalizing over the available volume defined as the total volume minus the volume occupied by two spheres of diameter σ and centered at the proteins' center of mass.
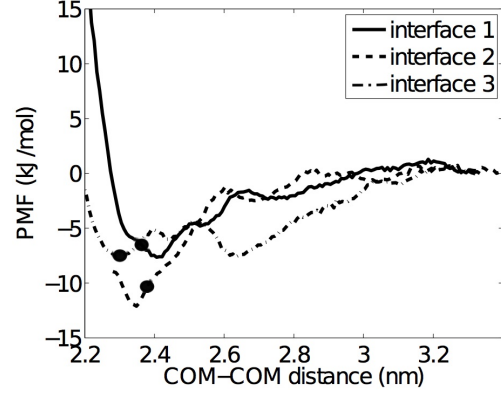

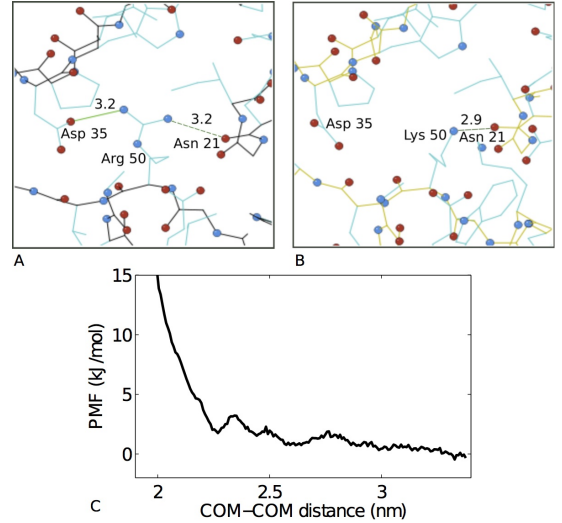FIG. A.8. PMF as a function of COM-COM distance for wt-RbPf in a 3 M solution of NaCl.

FIG. A.9. A: zoom on the interaction between Arg50 and the neighboring chain in interface 1 in mut-RbPa. The solid line identifies the salt-bridge with Asp35 and the dashed line the hydrogen bond with the carbonyl group of Asn21. B: interaction of Lys50 with the neighboring chain after deleting the last residue of wt-RbPf and fitting the structure in order to overlap the crystal contact of mut-RbPa. The Lysine can either form the hydrogen bond or the salt-bridge, but not both. Bond lengths (in Å) are reported above the bond lines. C: PMF for the interface represented in panel B, showing a neutral interaction between the two chains.

Appendix C: Determination of the phase diagram

The phase diagram is determined using advanced Monte Carlo (MC) techniques. Gibbs Ensemble MC simulations directly determine the coexistence densities of the metastable gas and liquid phases [67]. We simulate a total of $N = 1000$ particles for 10^6 MC cycles where each cycle consists on average of N particle displacements, N particle rotations, $N/10$ particle swaps, and 2 volume V changes. The critical temperature T_c and density are then estimated using the law of rectilinear diameters [68].

Because the gas-liquid line is metastable, we observe that for certain models crystallization happens so quickly that we are unable to determine the gas and liquid densities. In such cases (i.e. wt-RbPf at 3M of NaCl), we estimate the critical temperature as the lowest temperature at which phase separation is not observed within 10^6 MC cycles, which gives an error of about 3 K on the position of the critical point.

To determine the fluid-solid coexistence curve, we integrate the Clausius-Clapeyron equation starting from one coexistence point using a fourth order predictor-corrector algorithm [29]. The temperature step size is $\Delta\beta = 0.05$ for wt-RbPf and mut-RbPf and $\Delta\beta = 0.02$ for mut-RbPa.

The coexistence point is determined using free energy calculations. The free energy of the fluid is computed using thermodynamic integration from the free energy of an ideal gas [57]. The free energy of the crystal is determined using for reference the Einstein crystal with fixed center of mass [77] with Hamiltonian

$$H^{\text{Ein}}(\xi_{\text{trans}}, \xi_{\text{or}}) = \xi_{\text{trans}} \sum_{i=1}^{N} (\mathbf{r}_i - \mathbf{r}_{i,0})^2 + \xi_{\text{or}} \sum_{i=1}^{N} f(\theta_i, \phi_i, \chi_i),$$

(C1)

where $f(\theta_i, \phi_i, \chi_i) = 1 - \cos(\psi_{i,1}) + 1 - \cos(\psi_{i,2})$, $(\theta_i, \phi_i, \chi_i)$ are the Euler angles describing the orientation of particle i and $\psi_{i,j}$ is the angle formed between

the vector defining patch j of particle i and the corresponding vector in the Einstein crystal. As explained in Ref. [57], the free energy of the reference Einstein crystal can then be written as

$$a_{\text{Ein}}^{\text{COM}} = a_{\text{trans}}^{\text{COM}} + a_{\text{or}}^{\text{COM}},$$

(C2)

where

$$\beta a_{\text{trans}}^{\text{COM}} = -\frac{3}{2}\frac{N-1}{N}\ln\left(\frac{\pi}{\beta\xi_{\text{trans}}}\right) - \frac{3}{2N}\ln N$$

(C3)

and

$$\beta a_{\text{or}}^{\text{COM}} = -\ln\left\{\frac{1}{8\pi^2}\int d\theta \sin(\theta)d\phi d\chi \exp[-\beta\xi_{\text{or}}f(\theta, \phi, \chi)]\right\}.$$

(C4)

The calculation of $a_{\text{trans}}^{\text{COM}}$ is straightforward, but that of $a_{\text{or}}^{\text{COM}}$ requires either a tedious numerical integration, as in Ref. [78], or an analytical approximation. We opt for the latter using a saddle point approximation, which is very efficient for high values of $\beta\xi_{\text{or}}$ such as those used here, because the integrand is sharply peaked. Defining $(\theta_0, \phi_0, \chi_0)$ as the reference orientation in the Einstein crystal and changing variable $\boldsymbol{\alpha} = (\cos(\theta), \phi, \chi)$ gives

$$\int d\theta \sin(\theta)d\phi d\chi \exp[-\beta\xi_{\text{or}}f(\boldsymbol{\alpha})] = \int d\boldsymbol{\alpha} \exp[-\beta\xi_{\text{or}}f(\boldsymbol{\alpha})] \approx$$

$$\approx \frac{\exp[-\beta\xi_{\text{or}}f(\boldsymbol{\alpha}_0)](2\pi)^{3/2}}{(\beta\xi_{\text{or}})^{3/2}\det(H[f(\boldsymbol{\alpha}_0)])^{1/2}} = \frac{(2\pi)^{3/2}}{(\beta\xi_{\text{or}})^{3/2}\det(H[f(\boldsymbol{\alpha}_0)])^{1/2}},$$

such that

$$\beta a_{\text{or}}^{\text{COM}} \approx \frac{3}{2}\ln(\beta\xi_{\text{or}}) + \frac{1}{2}\ln(8\pi \det(H[f(\boldsymbol{\alpha}_0)])), \quad \text{(C5)}$$

where $\det(H[f(\boldsymbol{\alpha}_0)])$ is the determinant of the Hessian of function f computed at $\boldsymbol{\alpha}_0$. The analytical expression of $f(\boldsymbol{\alpha})$ is reported below defining $y = \cos(\theta)$ and ζ as the angle between the vectors identifying patch 1 and 2, which does not depend on the orientation of the particle.

$$\begin{aligned}
f(\boldsymbol{\alpha}) = \frac{1}{2}\Big\{ &4 - 3\sqrt{1-y^2}\cos(\phi)\cos(\phi_0)\sin(\theta_0) - \sqrt{1-y^2}\cos(\chi)\cos(\chi_0)\sin(\theta_0) - 2\sqrt{1-y^2}\cos(\phi)\cos(\zeta)\sin(\phi_0)\sin(\chi_0)\sin(\zeta) \\
&- 2y\cos(\chi_0)\cos(\zeta)\sin(\theta_0)\sin(\zeta)2y\cos(\phi)\cos(\chi)\sin(\phi_0)\sin(\chi_0)\sin^2(\zeta) - 2y\cos(\phi)\cos(\phi_0)\sin(\chi)\sin(\chi_0)\sin^2(\zeta) \\
&- \sqrt{1-y^2}\cos(\chi)\cos(\chi_0)\sin(\theta_0)\sin^2(\zeta) + y\cos(\phi)\cos(\phi_0)\cos(\chi)\sin(\theta_0)\sin(2\zeta) + \cos(\phi)\sin(\phi_0)\sin(\chi)\sin(\theta_0)\sin(2\zeta) \\
&+ \cos(\theta_0)\big[-3y + \cos(\phi_0)\cos(\chi_0)\sin(\phi)\sin(\chi) + \cos^2(\zeta)\left(-y + y\cos(\chi)\cos(\chi_0)\sin(\phi)\sin(\phi_0)\right) \\
&- \cos(\phi_0)\cos(\chi_0)\sin(\phi)\sin(\chi)) - 2\sqrt{1-y^2}\cos(\chi)\cos(\zeta)\sin(\zeta) + y\sin^2(\zeta) + \cos(\phi_0)\cos(\chi_0)\sin(\phi)\sin(\chi)\sin^2(\zeta) \\
&- 2\cos(\phi)\cos(\chi_0)\sin(\phi_0)\sin(\chi)\sin^2(\zeta) - y\cos(\chi)\cos(\chi_0)\left(2\cos(\phi)\cos(\phi_0)\sin(\zeta) + \sin(\phi)\sin(\phi_0)(1 + \sin^2(\zeta))\right) \\
&+ \sqrt{1-y^2}\cos(\phi)\cos(\phi_0)\cos(\chi_0)\sin(2\zeta) + \sqrt{1-y^2}\cos(\chi_0)\sin(\phi)\sin(\phi_0)\sin(2\zeta)\big] \\
&+ \sin(\phi)\big[-\sin(\phi_0)\left(2\sin(\chi)\sin(\chi_0)\sin^2(\zeta)\right) + \cos(\phi_0)\left(-2\cos(\zeta)\sin(\chi)\sin(\theta_0)\sin(\zeta)\right) \\
&+ \sin(\chi_0)\left(-2y\cos(\chi)\sin^2(\zeta) + \sqrt{1-y^2}\sin(2\zeta)\right)\big)\big]\Big\}.
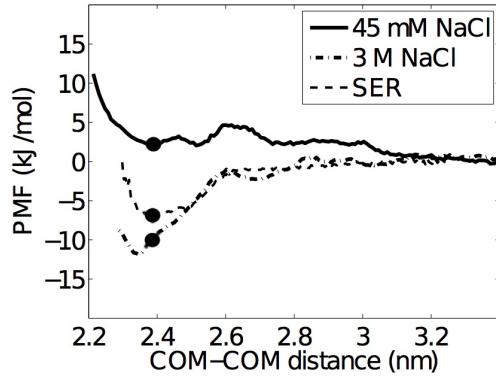\end{aligned}$$

FIG. A.10. Comparison between the effect of salt and the effect of the surface entropy reduction (SER) method on interface 1b. Following Ref. [27], we characterize the SER PMF on the E30A/E31A/E49A mutant of RbPf at 45 mM of NaCl, confirming that the interaction is attractive. Nevertheless, the interaction is weaker at high salt concentration, suggesting that the main contribution comes from the removal of the charged Glu49, not from entropy reduction (see Discussion).

Once the free energy of the reference crystal is known, the free energy of the actual crystal is calculated following the standard protocol [78]. Several simulations along an isobar starting from the fluid and from the crystal are then necessary to determine the temperature at which the chemical potential of the two phases coincides [57, 78]. The details of the coexistence points are reported in Table A.2.

Protein model	T	P	ρ_{fluid}	ρ_{crystal}
wt-RbPf	0.71	0.35	0.45	0.85
mut-RbPf	0.35	0.35	0.59	0.88
mut-RbPa	1.18	0.35	0.48	0.71

TABLE A.2. Temperature-pressure reference coexistence point between the fluid and the crystal for wt-RbPf, mut-bPf and mut-RbPa, where T and P stand for temperature (in 300 K) and pressure (in $k_B T/\sigma^3$) and ρ_{fluid} and ρ_{crystal} stand for the fluid and crystal density (in σ^{-3}), respectively.

[1] T. L. Blundell, H. Jhoti, and C. Abell, Nat Rev Drug Discov **1**, 45 (2002).
[2] D. B. Kitchen, H. Decornez, J. R. Furr, and J. Bajorath, Nat Rev Drug Discov **3**, 935 (2004).
[3] N. Huebsch and D. J. Mooney, Nature **462**, 426 (2009).
[4] T. M. Schmeing and V. Ramakrishnan, Nature **461**, 1234 (2009).
[5] J. A. Dunkle, L. Wang, M. B. Feldman, A. Pulk, V. B. Chen, G. J. Kapral, J. Noeske, J. S. Richardson, S. C. Blanchard, and J. H. D. Cate, Science **332**, 981 (2011).
[6] S. Grzesiek and H.-J. Sass, Curr Opin in Struct Biol **19**, 585 (2009).
[7] A. McPherson, *Crystallization of Biological Macromolecules* (CSHL Press, Cold Spring Harbor, 1999).
[8] N. E. Chayen and E. Saridakis, Nature Methods **5**, 147 (2008).
[9] N. E. Chayen, "High-throughput protein crystallization," in *Advances in Protein Chemistry and Structural Biology*, Vol. 77, edited by J. Andrzej (Academic Press, London, 2009) pp. 1–22.
[10] Z. Derewenda, Acta Crystallogr D Biol Crystallogr **66**, 604 (2010).
[11] M. J. Anderson, C. L. Hansen, and S. R. Quake, Proc Natl Acad Sci USA **103**, 16746 (2006).
[12] E. Saridakis and N. E. Chayen, Trends Biotechnol **27**, 99 (2009).
[13] J. N. Israelachvili, *Intermolecular and surface forces* (Academic Press, San Diego, 1991).
[14] D. Chandler, Nature **437**, 640 (2005).
[15] J. D. Gunton, A. Shiryayev, and D. L. Pagan, *Protein Condensation* (Cambridge University Press, 2007).
[16] S. Granick and S. C. Bae, Science **322**, 1477 (2008).
[17] B. J. Berne, J. D. Weeks, and R. Zhou, Annu Rev Phys Chem **60**, 85 (2009).
[18] P. G. Vekilov and A. A. Chernov, Solid State Physics **57**, 1 (2002).
[19] J. Janin, Prog Biophys Mol Biol **64**, 145 (1995).
[20] J. P. K. Doye, A. A. Louis, and M. Vendruscolo, Physical Biology **1**, P9 (2004).
[21] J. Janin and F. Rodier, Proteins **23**, 580 (1995).
[22] O. Carugo and P. Argos, Protein Sci **6**, 2261 (1997).
[23] R. P. Bahadur, P. Chakrabarti, F. Rodier, and J. Janin, J Mol Biol **336**, 943 (2004).
[24] M. Cieslik and Z. S. Derewenda, Acta Crystallogr D Biol Crystallogr **65**, 500 (2009).
[25] W. N. Price, Y. Chen, S. K. Handelman, H. Neely, P. Manor, R. Karlin, R. Nair, J. F. Liu, M. Baran, J. Everett, S. C. N. Tong, F. Forouhar, S. S. Swaminathan, T. Acton, R. Xiao, J. R. Luft, A. Lauricella, G. T. DeTitta, B. Rost, G. T. Montelione, and J. F. Hunt, Nat Biotechnol **27**, 51 (2009).
[26] Z. S. Derewenda and P. G. Vekilov, Acta Crystallogr D Biol Crystallogr **62**, 116 (2006).
[27] L. Goldschmidt, D. R. Cooper, Z. S. Derewenda, and D. Eisenberg, Protein Sci **16**, 1569 (2007).
[28] A. P. Gast, C. K. Hall, and W. B. Russel, J Colloid Interface Sci **96**, 251 (1983).
[29] M. H. J. Hagen and D. Frenkel, J Chem Phys **101**, 4093 (1994).
[30] A. Lomakin, N. Asherie, and G. B. Benedek, J Chem Phys **104**, 1646 (1996).
[31] D. Rosenbaum, P. C. Zamora, and C. F. Zukoski, Phys Rev Lett **76**, 150 (1996).
[32] N. E. Chayen, Progr Biophys Mol Biol **88**, 329 (2005).
[33] P. J. Lu, E. Zaccarelli, F. Ciulla, A. B. Schofield, F. Sciortino, and D. A. Weitz, Nature **453**, 499 (2008).
[34] P. R. ten Wolde and D. Frenkel, Science **277**, 1975 (1997).
[35] O. Galkin and P. G. Vekilov, Proc Natl Acad Sci USA **97**, 6277 (2000).
[36] V. J. Anderson and H. N. W. Lekkerkerker, Nature **416**, 811 (2002).
[37] A. George and W. W. Wilson, Acta Crystallogr D Biol

Crystallogr **50**, 361 (1994).

[38] C. Haas, J. Drenth, and W. W. Wilson, J Phys Chem B **103**, 2808 (1999).

[39] R. A. Curtis, H. W. Blanch, and J. M. Prausnitz, J Phys Chem B **105**, 2445 (2001).

[40] A. Lomakin, N. Asherie, and G. B. Benedek, Proc Natl Acad Sci USA **96**, 9465 (1999).

[41] J. J. McManus, A. Lomakin, O. Ogun, A. Pande, M. Basan, J. Pande, and G. B. Benedek, Proc Natl Acad Sci USA **104**, 16856 (2007).

[42] C. Gögelein, G. Nägele, R. Tuinier, T. Gibaud, A. Stradner, and P. Schurtenberger, J Chem Phys **129**, 085102 (2008).

[43] E. Bianchi, R. Blaak, and C. N. Likos, Phys Chem Chem Phys **13**, 6397 (2011).

[44] N. Kern and D. Frenkel, J Chem Phys **118**, 9882 (2003).

[45] P. Charbonneau and D. Frenkel, J Chem Phys **126**, 196101 (2007).

[46] G. Foffi and F. Sciortino, J Phys Chem B **111**, 9702 (2007).

[47] G. Pellicane, G. Smith, and L. Sarkisov, Phys Rev Lett **101**, 248102 (2008).

[48] R. Bau, D. C. Rees, D. M. Kurtz, R. A. Scott, H. S. Huang, M. W. W. Adams, and M. K. Eidsness, J Biol Inorg Chem **3**, 484 (1998).

[49] T. Chatake, K. Kurihara, I. Tanaka, I. Tsyba, R. Bau, F. E. Jenney, M. W. W. Adams, and N. Niimura, Acta Crystallogr D Biol Crystallogr **60**, 1364 (2004).

[50] H. Bonisch, C. L. Schmidt, P. Bianco, and R. Ladenstein, Acta Crystallogr D Biol Crystallogr **61**, 990 (2005).

[51] A. De Simone, C. Kitchen, A. H. Kwan, M. Sunde, C. M. Dobson, and D. Frenkel, Proc Natl Acad Sci USA (2012).

[52] Y.-E. A. Ban, H. Edelsbrunner, and J. Rudolph, J ACM **53**, 361 (2006).

[53] S. D. Black and D. R. Mould, Anal Biochem **193**, 72 (1991).

[54] J. J. Headd, Y. E. Ban, P. Brown, H. Edelsbrunner, M. Vaidya, and J. Rudolph, J Proteome Res **6**, 2576 (2007).

[55] P. Bash, U. Singh, R. Langridge, and P. Kollman, Science **236**, 564 (1987).

[56] R. P. Sear, J Chem Phys **111**, 4800 (1999).

[57] C. Vega, E. Sanz, J. L. F. Abascal, and E. G. Noya, J Phys Cond Matter **20**, 153101 (2008).

[58] T. K. Haxton and S. Whitelam, Soft Matter **8**, 3558 (2012).

[59] R. Zangi, M. Hagen, and B. J. Berne, J Am Chem Soc **129**, 4678 (2007).

[60] C. J. Lanci, C. M. MacDermaid, S.-g. Kang, R. Acharya, B. North, X. Yang, X. J. Qiu, W. F. DeGrado, and J. G. Saven, Proc Natl Acad Sci USA **109**, 7304 (2012).

[61] N. Giovambattista, P. G. Debenedetti, and P. J. Rossky, J Phys Chem C **111**, 1323 (2006).

[62] L. Vega, E. d. Miguel, L. F. Rull, G. Jackson, and I. A. McLure, The Journal of Chemical Physics **96**, 2296 (1992).

[63] B. Hess, C. Kutzner, D. van der Spoel, and E. Lindahl, J Chem Theory Comput **4**, 435 (2008).

[64] V. Hornak, R. Abel, A. Okur, B. Strockbine, A. Roitberg, and C. Simmerling, Proteins **65**, 712 (2006).

[65] W. L. Jorgensen, J. Chandrasekhar, J. D. Madura, R. W. Impey, and M. L. Klein, J Chem Phys **79**, 926 (1983).

[66] J. S. Hub, B. L. de Groot, and D. van der Spoel, J Chem Theory Comput **6**, 3713 (2010).

[67] A. Z. Panagiotopoulos, Mol Phys **61**, 813 (1987).

[68] D. Frenkel and B. Smit, *Understanding Molecular Simulation* (Academic Press, London, 2001).

[69] GJ Kleywegt, Uppsala University, Uppsala, Sweden, unpublished program. Url: http://xray.bmc.uu.se/usf/xutil.html.

[70] W. M. Westler, I.-J. Lin, A. Perczel, F. Weinhold, and J. L. Markley, JACS **133**, 1310 (2011).

[71] P. R. Blake, J. B. Park, Z. H. Zhou, D. R. Hare, M. W. Adams, and M. F. Summers, Protein Sci **1**, 1508 (1992).

[72] P. Bjelkmar, P. Larsson, M. Cuendet, B. Hess, and E. Lindahl, JCTC **6**, 459 (2010).

[73] O. Carugo and K. D. Carugo, Trends in Biochemical Sciences **30**, 213 (2005).

[74] Y. Shen and A. Bax, J Biomol NMR **38**, 289 (2007).

[75] J. J. Gray, S. Moughon, C. Wang, O. Schueler-Furman, B. Kuhlman, C. A. Rohl, and D. Baker, J Mol Biol **331**, 281 (2003).

[76] S. Chaudhury, A. Sircar, A. Sivasubramanian, M. Berrondo, and J. J. Gray, Proteins **69**, 793 (2007).

[77] D. Frenkel and A. J. C. Ladd, J Chem Phys **81**, 3188 (1984).

[78] F. Romano, E. Sanz, and F. Sciortino, J Chem Phys **132**, 184501 (2010).